On Linear and Nonlinear Aspects of Dynamic Mode Decomposition

A.K. Alekseev[1], D.A. Bistrian[2], A.E. Bondarev[3] and I.M. Navon[4*]

[1]*Moscow Institute of Physics and Technology, Moscow, Russia*
[2]*Department of Electrical Engineering and Industrial Informatics, University"Politehnica" of Timisoara, 331128 Hunedoara, Romania*
[3]*Keldysh Institute of Applied Mathematics RAS, Moscow, Russia*
[4]*Department of Scientific Computing, Florida State University, Tallahassee, FL 32306-4120*

SUMMARY

The approximation of reduced linear evolution operator (propagator) via Dynamic Mode Decomposition is addressed for both linear and nonlinear events. The 2D unsteady supersonic underexpanded jet, impinging the flat plate in nonlinear oscillating mode, is used as the first test problem for both modes. Large memory savings for the propagator approximation are demonstrated. Corresponding prospects for the estimation of receptivity and singular vectors are discussed. The shallow water equations are used as the second large scale test problem. Excellent results are obtained for the proposed optimized DMD method of the shallow water equations when compared with recent POD/DEIM based model results in the literature.

KEYWORDS: dynamic mode decomposition; propagator; unsteady Euler equations, shallow water equations.

1. INTRODUCTION

The Dynamic Mode Decomposition (DMD) is a recently devised method for the search of a small number of basis vectors (dynamic modes) able to describe the total fluid state [1-12]. It promises certain advance in the retrieval of flow structures which provide a low dimensional approximation of complex unsteady flowfields. DMD is based on an algorithm for numerical estimation of eigenvalues Λ and right eigenvectors Ω_R of an operator A determining the flow evolution (linear propagator). The set of flow snapshots is used as the input data.

A powerful way of analyzing nonlinear flow dynamics using linear techniques is provided by the use of dynamic modes (see e.g. the work of Holmes et al. [7], Bagheri [8], Mezic [9]). Among several snapshot-based modal decomposition methods, dynamic mode decomposition (DMD) have been widely applied to study the physics of the dynamics of the flows in different applications.

A theoretical framework is proposed by Tu et al. [10], in which DMD is defined as the eigendecomposition of an approximating linear operator. They demonstrate the utility of this approach by presenting novel sampling strategies that increase computational efficiency and mitigate the effects of noise. A new technique that allows dynamical information to be extracted from large datasets and data streams is proposed by Hemati et al. [11]. Their low-storage method for performing dynamic mode decomposition can be updated inexpensively as new data become available. The problem of modal decomposition of large and arbitrarily sampled systems is addressed by Guéniat et al. [4]. Their method essentially formulates the problem in an optimization setting and decouples the estimation of the temporal description from the spatial description.

In a bold manner, the problem of systems governed by nonlinear evolution laws is addressed by Williams and his coworkers [12]. They demonstrate that the Koopman eigenfunctions and eigenvalues define a set of intrinsic coordinates, which serve as a natural framework for fusing measurements obtained from heterogeneous collections of sensors.

Correspondence to: Dirac Science Library Building, Florida State University, Tallahassee, FL 32306-4120.
E-mail: inavon@fsu.edu

In the present paper we denote the operator A as the Schmid operator (which acts on dynamic variables) in order to distinguish it from the Koopman operator [2, 13, 14] (which acts on observable variables).

The DMD approach enables one to obtain also a set of left eigenvectors Ω_L. This set provides the feasibility to approximate the Schmid operator as a product of the diagonal and two rectangular matrices $A = \Omega_R \Lambda \Omega_L$. In this form the Schmid operator A may be efficiently stored and used implicitly.

The matrix form of Schmid operator A is interesting for several important classes of problems. For example, the adjoint propagator A^* is used in receptivity problems [15]. The actions of operator A^*A are used for the maximal eigenvalue estimation. The corresponding eigenvector provides the most rapidly growing perturbations at a finite time interval (singular vectors [16]) that are also of current interest.

The evaluation of receptivity and the estimation of the singular vectors are both linear problems. If flow dynamics is nonlinear, the linear approximation may be based on a short time interval between snapshots.

DMD also may be applied to essentially nonlinear problems [2]. The physical meaning of the operator changes for longer time intervals (providing nonlinearity); at some limit the operator may become independent of the snapshots selection and may be considered as a form of the Koopman operator.

The remainder of this article is organized as follows. In Section 2 we present one of the main version of DMD in accordance with [1] along with some of its properties especially useful for our purposes. Section 3 considers the construction of the Schmid operator as a product of rectangular matrices and the equivalence of DMD and Schmid operator. Section 4 analyses the relations between the Schmid operator and the propagator (flow evolution operator) in both linear and nonlinear modes. Further, in Section 5, the numerical test results of the Schmid operator estimation in linear and nonlinear modes are presented. A supersonic jet interaction with the flat surface is considered as one of the test problem. The second test problem concerns flows described by shallow water equations. Several problems, having prospects for the Schmid operator applications, are surveyed in Section 6. Conclusions are drawn and presented in the final Section 7.

2. DMD VERSION FOR NON-NORMALIZED MODES

There exist several approaches to DMD construction that include: normalized dynamic modes [1], non-normalized dynamic modes [2, 6] and optimization over eigenvalues [3, 4]. In the present paper, it is more convenient from our purposes to use normalized modes. So, herein, we consider the main features of DMD in accordance with [1]. Let's consider a set of N snapshots $Sn_1^N = (u_1 ... u_N)$, which are discrete approximations of the flow fields at consecutive time instances separated by an identical interval Δt. Each snapshot u_i is a vector of the dimension Nt. The linear operator $A(\Delta t)$ (an unknown matrix of dimension $Nt \times Nt$) is assumed to exist and provide the transformation $u_{i+1} = Au_i$. In this case the snapshots form a Krylov sequence $Sn_1^N = \{u_1, Au_1, A^2u_1, ..., A^{N-1}u_1\}$.

For a long enough snapshot set, the eigenvalues and right eigenvectors $Av_j = \lambda_j v_j$ may be calculated and the snapshots may be written as

$$u_k = \sum_j a_j v_j \lambda^{k-1} = \sum_j a_j v_j e^{(\sigma_j + i\omega_j)(k-1)\Delta t}, \ (k = 1, N). \tag{1}$$

Usually, the right eigenvectors $v_j \in C$ are denoted as dynamic (Koopman) modes, the eigenvalues $\lambda_j \in C$ are denoted as (Koopman) eigenvalues, and the coefficients $a_i \in C$ are denoted as amplitudes (Koopman eigenfunctions).

The estimation of Koopman modes, eigenvalues and amplitudes from the known set of snapshots Sn_1^N is the main computational problem from this viewpoint. The sets of shifted snapshots $Sn_1^{N-1} = (u_1 ... u_{N-1}) = (u_1 ... A^{N-2} u_1)$, $Sn_2^N = (u_2 ... u_N) = A Sn_1^{N-1}$ are used, herein, according to [1]. The set Sn_1^N is assumed to capture the main physical features of a considered process more precisely as the number of snapshots increases. If a certain critical number of snapshots is exceeded, the following snapshots should become linearly dependent on the previous ones (similar to Krylov type iteration processes). In this limit, the last snapshot u_N may be expressed via the previous snapshots with some error r:

$$u_N = c_1 u_1 + c_2 u_2 + ... + c_{N-1} u_{N-1} + r. \tag{2}$$

By substituting u_N in Sn_2^N and using a companion matrix C, we obtain $Sn_2^N = Sn_1^{N-1} \cdot C + r$, where

$$C = \begin{pmatrix} 0 & & & c_1 \\ 1 & 0 & & c_2 \\ & 1 & 0 & \\ & & \dots & \dots \\ & & & 1 \quad c_{N-1} \end{pmatrix}. \tag{3}$$

The expression $Sn_2^N \approx Sn_1^{N-1} \cdot C$ holds under the assumption of small r. Thus, it can be stated that:

$$A \cdot Sn_1^{N-1} = Sn_2^N = Sn_1^{N-1} \cdot C. \tag{4}$$

The set of snapshots may be presented using SVD [17] as follows:

$$Sn_1^{N-1} = U \Sigma V^*. \tag{5}$$

Since the snapshot matrix is not invertible, the Moore-Penrose pseudoinverse matrix for Sn_1^{N-1} is used which can be written as $V \Sigma^+ U^*$. We denote here $\Sigma^+ = diag(\sigma_1^{-1}, ..., \sigma_r^{-1}, 0, ...0)$.

From the expression $Sn_2^N = Sn_1^{N-1} C$ one may obtain via the pseudoinverse matrix:

$$C = V \Sigma^+ U^* Sn_2^N. \tag{6}$$

Let us change the companion matrix C by the transformation**:**

$$\tilde{C} = (V \Sigma^+)^{-1} C (V \Sigma^+). \tag{7}$$

Under this transformation, eigenvalues do not change, while the eigenvectors are rotated: $y^C = V \Sigma^+ y^{\tilde{C}}$, $y^{\tilde{C}} = \Sigma V^* y^C$.

Further, the substitution of expression (6) into (7) yields**:**

$$\tilde{C} = U^* Sn_2^N V \Sigma^+. \tag{8}$$

From $A \cdot Sn_1^{N-1} = Sn_1^{N-1} \cdot C$ one may obtain $A \cdot U \Sigma V^* = U \Sigma V^* \cdot C$, $A \cdot U = U \Sigma V^* \cdot C \cdot (\Sigma V^*)^{-1}$ and $A \cdot U = U \tilde{C}$. Taking into account $\tilde{C} = W \Lambda W^{-1}$ ($W = \Omega_R^{\tilde{C}}$) we obtain the expression

$$A \cdot UW = UW \cdot \Lambda. \tag{9}$$

One can see from (9) that the eigenvalues Λ of the matrix $\tilde{C}$ coincide with the eigenvalues of A. The right eigenvector of A assumes the form:

$$\Omega_R^A = UW = U \Omega_R^{\tilde{C}}. \tag{10}$$

Since the matrix C is not symmetric, the right eigenvectors do not form an orthogonal basis and the set of left eigenvectors (biorthogonal to right) is necessary. They may be obtained from the expression $A \cdot Sn_1^{N-1} = Sn_1^{N-1} \cdot C$ via SVD decomposition of the snapshot set $A \cdot U \Sigma V^* = U \Sigma V^* \cdot C$**.** Further, the chain of transformations $V \Sigma^+ U^* \cdot A \cdot U \Sigma V^* = C$ $V \Sigma^+ U^* \cdot A = C \cdot V \Sigma^+ U^*$ provides the

expression $U^* \cdot A = (V\Sigma^+)^{-1} \cdot C \cdot V\Sigma^+ U^* = \tilde{C}U^*$. Taking into account the $\tilde{C}$ eigenvector decomposition, we get $U^* \cdot A = W\Lambda W^{-1}U^*$ and obtain $W^{-1}U^* \cdot A = \Lambda W^{-1}U^*$ that determines the left eigenvector of A:

$$\Omega_L^A = W^{-1}U^* = \Omega_L^{\tilde{C}}U^*. \tag{11}$$

This enables an expansion in the series over the right eigenvectors ($u_1 = a_j v_j$). The coefficients a_j may be calculated via the biorthogonality relation (l_i is the left eigenvector that belongs to Ω_L^A matrix)

$$v_k l_i^* = \delta_{ik} \tag{12}$$

and has the form

$$a_k = (l_k^* u). \tag{13}$$

3. THE REDUCED FORM OF THE SCHMID OPERATOR

Thus, the eigenvalues and (right and left) eigenvectors of the Schmid operator A may be estimated from the spectrum of matrix $\tilde{C} = U^* S n_2^N V\Sigma^+$. Then, the construction of the Schmid operator in the following reduced form is feasible:

$$A = \Omega_R^A \Lambda \Omega_L^A, \tag{14}$$

where Ω_R^A, Ω_L^A are rectangular matrices and Λ is a diagonal one.

The explicit form of propagator matrix A requires very high memory of dimension about $Nt \times Nt$ for CFD applications. Even for moderate grids (for example, about 100 nodes over a single spatial coordinate) $Nt \sim 4 \times 10^4$ in the 2D case and $Nt \sim 5 \times 10^6$ in 3D case. The decomposition of A via a product of reduced matrices requires the storage of only $2Nt \times N + N$ numbers. In the 2-D case for $Nt \sim 4 \times 10^4$ and $N \sim 40$, the memory saving is about three orders of magnitude. The CPU time savings are close or more significant due to the nonlinear growth of the computer time necessary for the spectrum estimation as the matrix order increases.

It should be stressed that calculations of snapshots by the reduced Schmid operator approximation $A = \Omega_R \Lambda \Omega_L$ and by DMD are equivalent:

$$u_k = (\Omega_R \Lambda \Omega_L)(\Omega_R \Lambda \Omega_L)...\Omega_R \Lambda (\Omega_L u_1) = (\Omega_R \Lambda \Omega_L)^{k-1} u_1 = \Omega_R \Lambda^{k-1} \Omega_L u_1 = \sum_{i=1}^{N} a_i v_i \lambda_i^{k-1}. \tag{15}$$

Thus, the analysis of the Schmid operator properties is directly applicable to the DMD method.

4. RELATIONS OF SCHMID OPERATOR AND PROPAGATOR

Let the dynamics of a system be described by the equation

$$du / dt = Bu. \tag{16}$$

In the analysis we use M steps of evolution between consecutive snapshots u_k, u_{k+1} with the step duration τ. Then the time interval between snapshots is $M\tau = \Delta t$.

Consider an approximation of the solution propagator and its relations with the Schmid operator for both linear and nonlinear events.

Linear case. If an operator B does not depend on u, then the propagator approximation may be written as the product of the single time step τ operators

$$L(\Delta t)u_1 = e^{\sum B\tau}u_1 = e^{\sum B\Delta t/M}u_1 = e^{B\Delta t}u_1 = A(\Delta t)u_1. \quad (17)$$

Thus, in the linear case, the Schmid operator is equivalent to the approximation of propagator $L(\Delta t) = A(\Delta t)$.

Nonlinear case. In general, a nonlinear propagator assumes the form

$$L(\Delta t)u_1 = e^{\sum B(u_k)\tau}u_1. \quad (18)$$

It essentially depends on the set of points between snapshots and, thus, is not invariant for different intervals and does not correspond to the Schmid operator properties.

However, if for some reason the propagator does not depend on intermediate points $u_n, u_2^* ... u_M^*, u_{n+1}$ between the snapshots u_n and u_{n+1}, for example, if there exists a mean operator

$$\bar{B} = \frac{1}{M}\sum_M B(u_k^*) \quad (19)$$

and it is invariant for all intervals, then:

$$Lu_n = e^{\sum B(u_k)\tau}u_n = e^{\bar{B}\Delta t}u_n = Au_n \quad (20)$$

and the propagator approximation $A = e^{\bar{B}\Delta t}$ may be considered as a Schmid operator.

Hence, there are two cases: linear and nonlinear ("averaged"), when such linear operator A may exist, that corresponds to the propagator L.

In the linear event the operator A_{ji} is estimated in vicinity of a single point of the dynamic system trajectory and implies a "linearization in small".

For the nonlinear asymptotic, the operator A_{ji} is defined on a large part of the system trajectory and may be considered as a "linearization in the large" [14].

5. NUMERICAL TESTS

Two large scale problems are used for the demonstration of abovementioned features of the reduced form of the Schmid operator approximation. The first problem concerns an unsteady flow of impinging jet described by the Euler equations. The second problem concerns flows described by the shallow water equations. Some numerical results are provided below.

5.1.1 2D jet impingement simulation

The subroutines DGESVD (LAPACK [21]) and SNAUPD, SNEUPD (ARPACK [22]) were used for SVD decomposition.

Subroutine DGEEV (LAPACK) was used for the calculation of complex eigenvalues, right and left eigenvectors of the non-symmetric companion type matrices.

The numerical tests were conducted both for the low dimensional problems with a-priori known matrix operator A and for a large scale problem for the Schmid operator computed from N snapshots, obtained from the numerical solution of the two dimensional Euler equations.

The original operator A was estimated from the set of its actions for low dimensional operators (from 5×5 to 10×10). Results of numerical tests confirmed the correct reconstruction of original operator A.

For a large scale problem, the Schmid operator was reconstructed via the product of the rectangular matrices $Nt \times N$, where $Nt = 36000$ and $N = 10 \div 50$.

At a normal impingement of supersonic underexpanded jet on a plate, the flow pattern depends on parameters such as the Mach number M_a, pressure ratio $n = p_0 / p_a$, and distance from

nozzle exit by the surface x / d_a. Within a rather narrow range of parameters, oscillating flow modes are known to occur. In this mode, the shock wave structure causes peripheral pressure maximums, which may lead to an unsteady separation. The results of computation of the oscillating flow seem to be appropriate as a test problem in order to test performance of DMD. Evidently, the influence of turbulence is neglected. However, the shock induced unsteady separation bubble may be successfully modeled by an inviscid numerical method providing a good agreement with the experimental data [18]. So, this model correctly represents a true nonlinear unsteady flow dynamics and is useful for DMD tests due to its low computational costs. The following 2D+1 Euler equations are used.

$$\frac{\partial \rho}{\partial t} + \frac{\partial (\rho U_k)}{\partial x^k} = 0, \tag{21}$$

$$\frac{\partial (\rho U_i)}{\partial t} + \frac{\partial (\rho U_k U_i + P\delta_{ik})}{\partial x^k} = 0, \tag{22}$$

$$\frac{\partial (\rho E)}{\partial t} + \frac{\partial (\rho U_k h_0)}{\partial x^k} = 0. \tag{23}$$

Here $U_i = (U,V)$ are the velocity components, $h_0 = (U^2 + V^2)/2 + h$, $h = \frac{\gamma}{\gamma - 1}\frac{P}{\rho} = \gamma e$, $e = \frac{RT}{\gamma - 1}$, $E = \left(e + (U^2 + V^2)/2\right)$ are enthalpies and energies (per unit volume) respectively, and $P = \rho RT$ is the state equation.

The computations are performed in the spatial domain $\Omega = (0 < x < X_{\max}, 0 < y < Y_{\max})$ during the time interval $(0 < t < t_f)$ with the flow snapshot recorded at equally spaced time subintervals Δt.

At the boundary $(x = 0)$, we accept the supersonic inflow conditions, corresponding a nozzle exit section and the environment conditions (pressure, temperature, zero normal derivatives of velocities) on another part of the boundary. At the right boundary a no penetration condition is set. On the lateral boundaries $(y = 0, y = Y_{\max})$ we impose the outflow conditions in the supersonic region and the environment conditions at the subsonic part of the boundary.

The Euler equations were solved by a method of second order spatial accuracy [19] with the numerical fluxes calculated via the method by Sun and Katayama [20] and a second order time discretization.

5.1.2. The gas dynamics features of the flow

The periodic formation and disappearance of a separation bubble is specific for this mode. Figures 1 and 2 demonstrate the density fields for the maximal and minimal (developed separation bubble) pressure and corresponding streamlines. Figure 3 provides the surface pressure variation in time at the axis of symmetry for the transitional and following oscillation modes. The results correspond to the flow parameters $M_a = 4.0$, $\gamma = 1.4$, $x / d_a = 15$, $n = 4$.

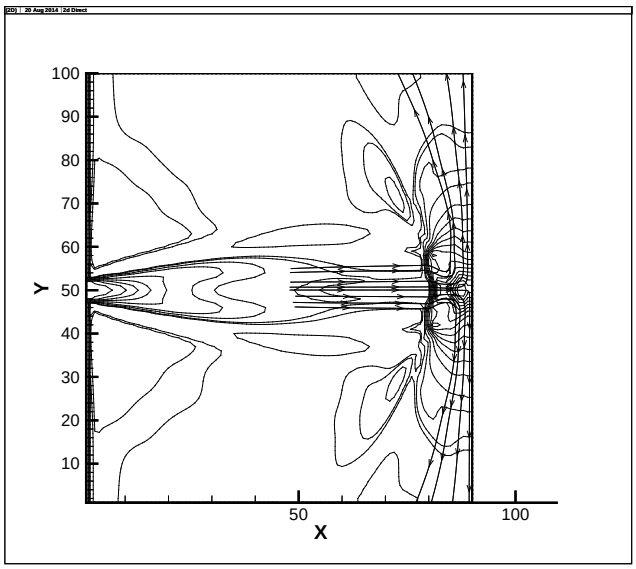

Figure 1. Density isolines and streamlines for the maximal pressure.

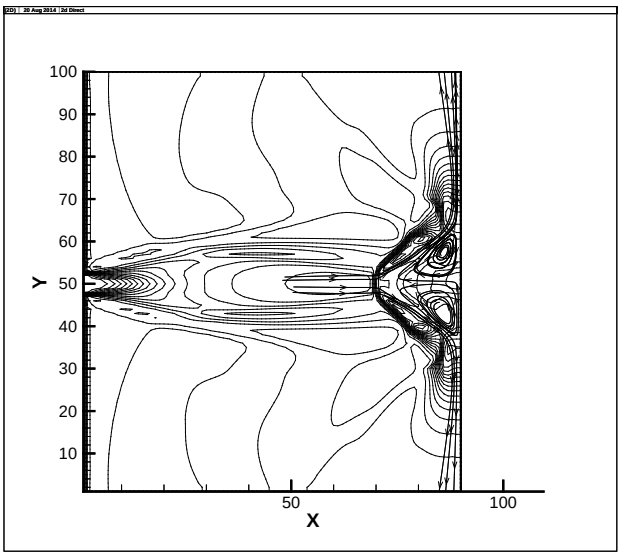

Figure 2. Density isolines and streamlines for the minimal pressure.

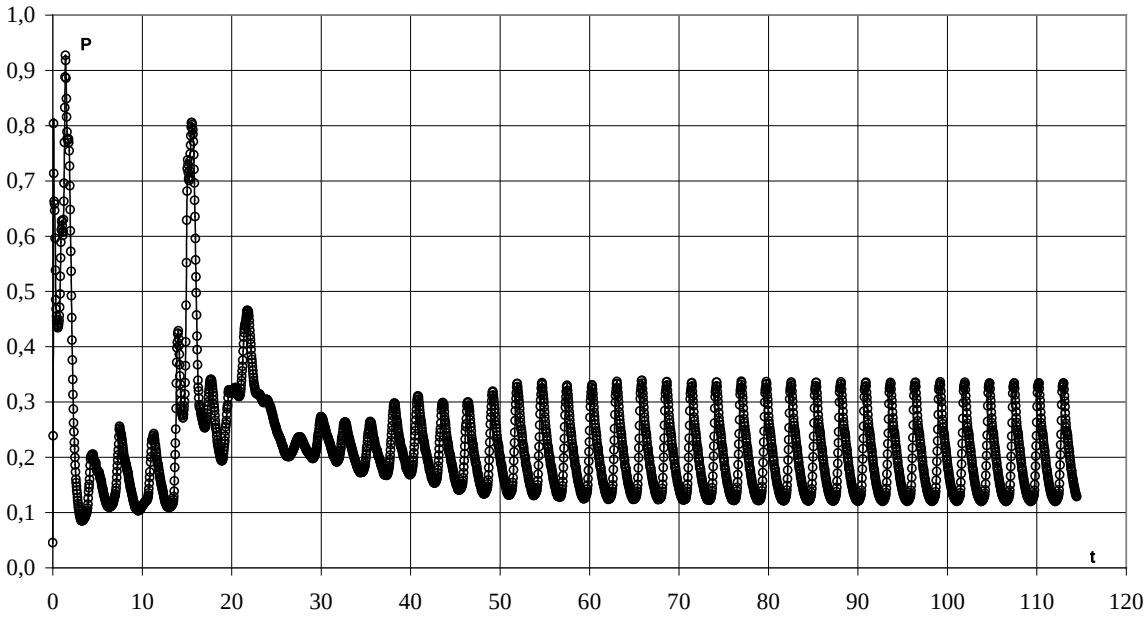

Figure 3. The pressure at the axis of symmetry as a function of dimensionless time.

5.1.3. DMD analysis for linear mode

The existence of a linear mode is expected for a small interval Δt between snapshots (several steps of the finite difference algorithm). The eigenvalues for linear problems, usually, are not located on the unit circle. Figure 4 presents the complex eigenvalues (dependence $\lambda_{\mathrm{Re}}(\lambda_{\mathrm{Im}})$) for the interval between snapshots of $\Delta t = 10$ and 15 steps, selected on the oscillations phase of evolution.

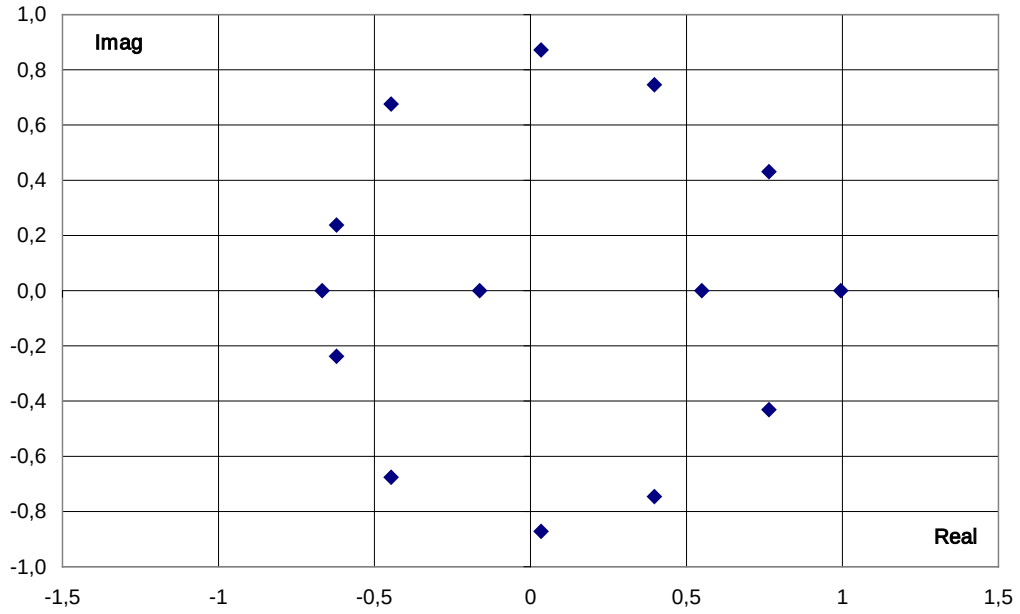

Figure 4. Eigenvalues $\lambda_{\mathrm{Re}}(\lambda_{\mathrm{Im}})$.

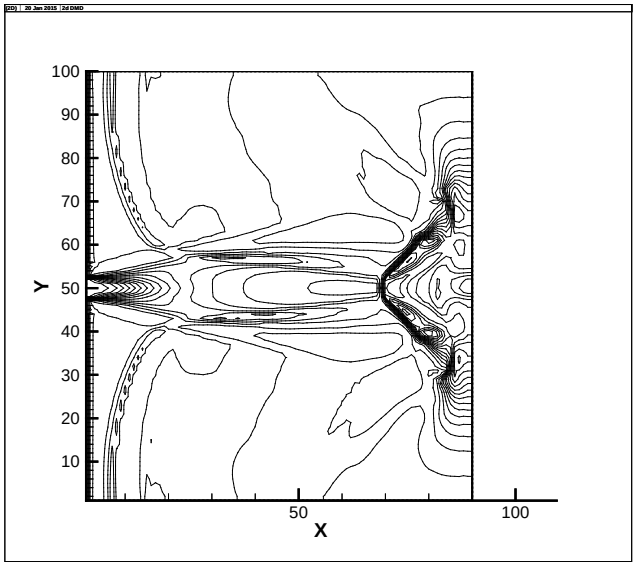

Figure 5. Isolines of right real eigenvector $\Omega_{R,1}$ for $k=5$.

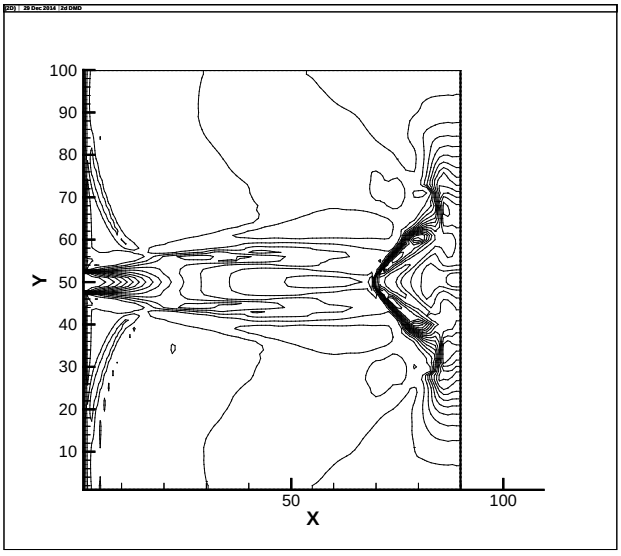

Figure 6. Isolines of right real eigenvector $\Omega_{R,1}$ for $k=10$.

Figures 5 and 6 illustrate the right real eigenvectors $\Omega_{R,1}$ (the component of density) for $\Delta t = k \cdot \tau$ ($k=5$ and 10 steps of CFD algorithm). One may see a relatively small variation of eigenvector structure at the time shift.

For $\Delta t = k \cdot \tau$ ($k=5$, 10) Figures 7 and 8 depict amplitudes $Amp(\Omega_{R,4})$ (also density component) for one of the right complex eigenvectors $v_k = Amp_k e^{i\phi_k}$.

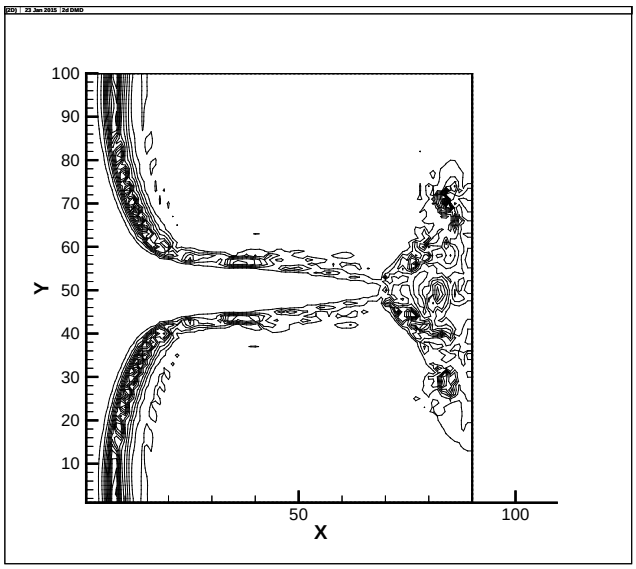

Figure 7. Isolines of right complex eigenvector amplitude $Amp(\Omega_{R,4})$ for $k=5$.

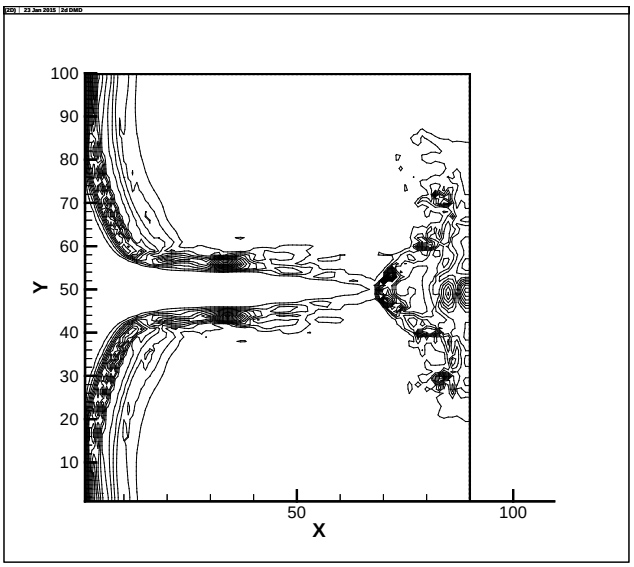

Figure 8. Isolines of right complex eigenvector amplitude $Amp(\Omega_{R,4})$ for $k=10$.

The variation of some eigenvalues as a function of the distance between the snapshots (number of time steps k) is provided in Figure 9. The eigenvalues are displayed for two real modes (lines 2 and 3). The phase shift α_4 is plotted for one of the complex modes (line 1). A linear dependence on k may be observed. The spectrum structure for the linear event is found to be stable.

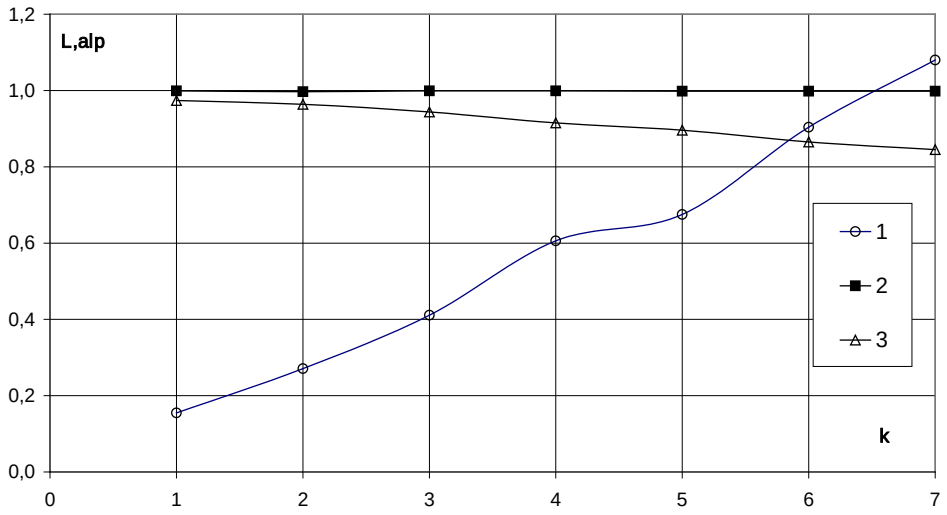

Figure 9. The real eigenvalues and the phase shift α_4 as functions of the number of time steps k . 1 is the phase shift α_4 , 2, 3- two real eigenvalues.

A comparison of the numerical results presented in Figure 5 to Figure 8 demonstrates a relatively small variation of right eigenvectors Ω_R over k , a similar behavior is also specific for the left eigenvectors Ω_L . Thus, in linear approach (at small distances Δt), the dynamics is determined by the variation of $\Lambda(\Delta t)$ at constant Ω_R and Ω_L . The evolution of flow, in this event, is caused by the rotation of constant eigenvectors in the complex plane.

At small intervals between snapshots (about single computation step) some ripples are visible in Ω_R and Ω_L. For $k \geq 5$ these ripples are practically invisible.

5.1.4. DMD analysis for nonlinear mode

Herein, only self-oscillating part of the flow history is used for tests due to its transparency. Figure 10 presents the dependence $\lambda_{\mathrm{Re}}(\lambda_{\mathrm{Im}})$ for time interval $\Delta t = 500$ steps which far deviates from the oscillation period ($T_{osc} \approx 780$ steps). In this test 40 snapshots are used. Eigenvalues are close to the unit circle that is common for nonlinear problems.

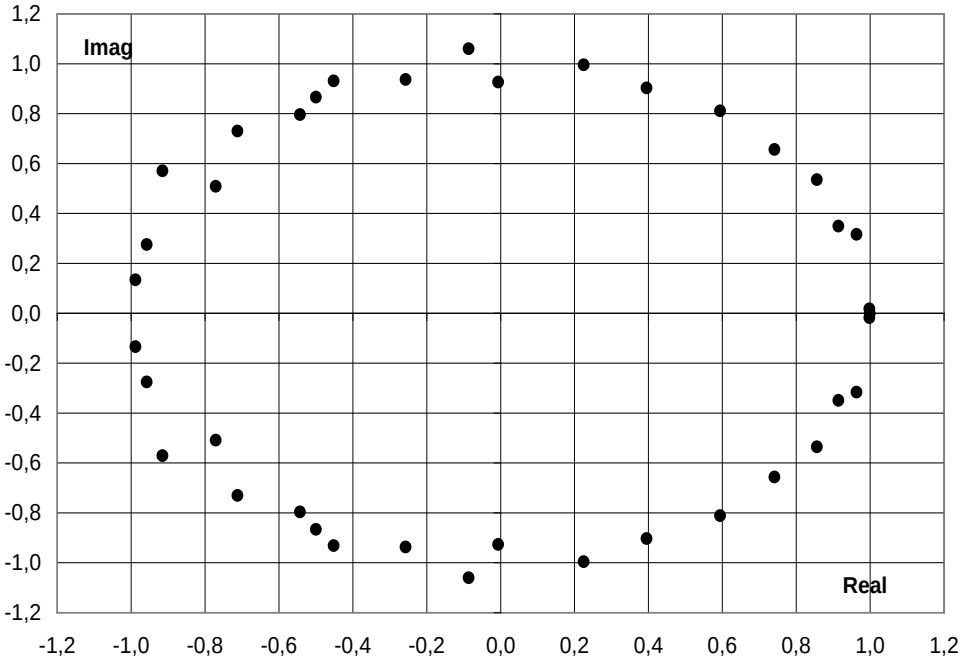

Figure 10. Eigenvalues $\lambda_{\mathrm{Re}}(\lambda_{\mathrm{Im}})$ for nonlinear mode.

Figure 11 shows the dependence of the amplitude on the frequency for 10 (line 1) and 40 (line 2) snapshots. The maximal amplitude correlates with the main frequency of oscillating mode ($\omega \approx 2.3$). Thus, DMD in nonlinear mode enables the capture of the main features of flow with highly nonlinear (due to shock waves) oscillations.

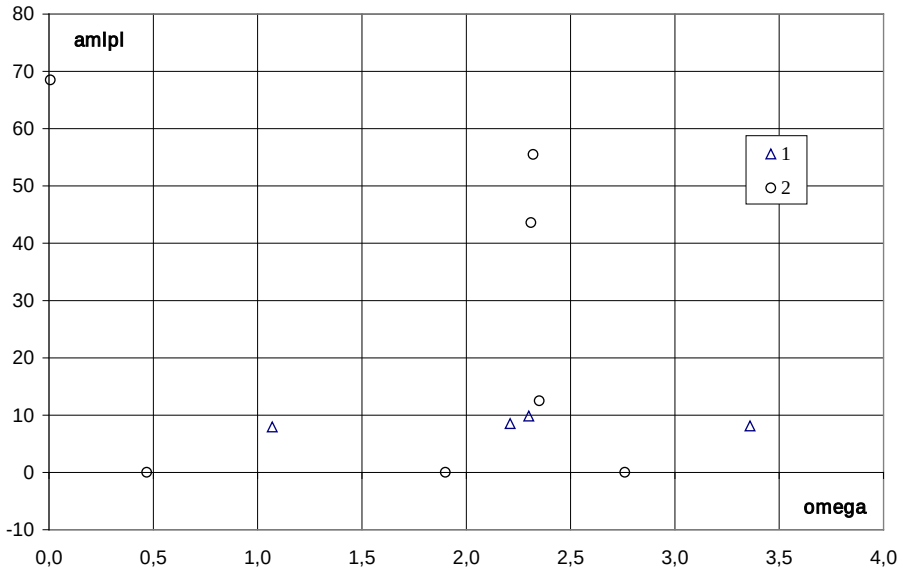

Figure 11. Amplitudes as a function of the optimal frequency estimations. 1 corresponds to 10 snapshots, 2 corresponds to 40 snapshots.

The quality of snapshot reconstruction may be estimated from Figures 12 and 13. Figure 12 represents one of snapshots (density field at separation stage, $k = 800$) and Figure 13 represents the result of the reconstruction at $k = 800$ performed using the rotation of eigenvectors obtained from data at $k = 760$.

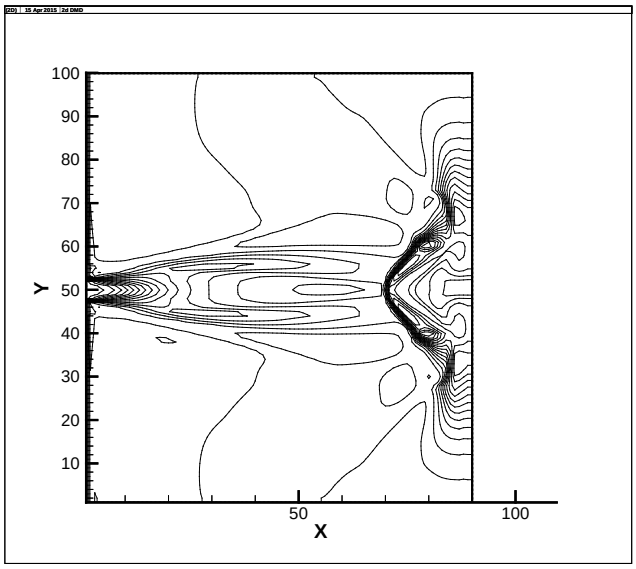

Figure 12. Density isolines for the snapshot that corresponds the separation stage.

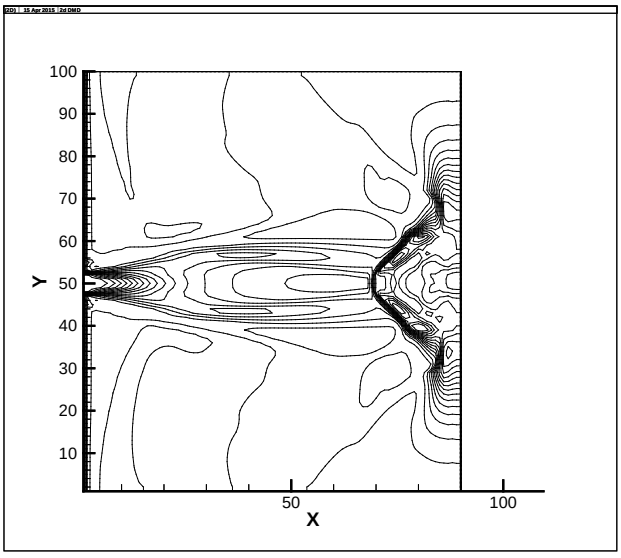

Figure 13. Reconstructed density isolines for the snapshot from Figure 14.

It should be noted, that the DMD results significantly depend on the number of snapshots. Figure 14 reveals the dependence of error norm $\|r\|$ (Eq. (2)) on the number of snapshots N in a logarithmic scale for nonlinear mode. A convergence with increasing number of snapshots N is observable, however, when N exceeds some number, the convergence deteriorates, a fact which may be attributed to the accumulation of numerical errors.

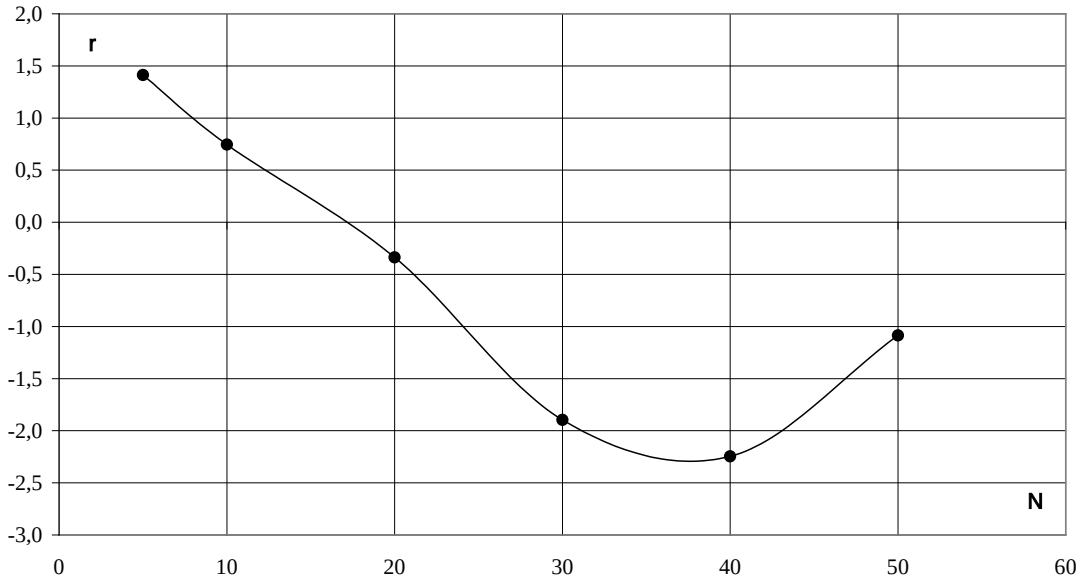

Figure 14. The error norm $\|r\|$ (Eq. (2)) as function of the number of snapshots N in logarithm scale.

Table 1 presents the computer time (Intel Core2Duo CPU, 3.0 GHz, 4.0 Gb) for different numbers of snapshots. The linear dependence is observable.

Table 1. CPU time T function of the number of snapshots N

N	10	20	30	40	50
T [sec]	52.3	142.1	182.0	247.8	301.6

However, the full scale problem ($N = Nt$, $Nt \sim 4 \cdot 10^4$) seems quite unsolvable both from memory (~100 Gb) and computer time (~3 months) considerations. In general, this result looks as very promising from the viewpoint of reduced order approximation.

5.2. DMD analysis of 2D shallow water dynamics

The shallow-water equations have been used for a wide variety of hydrological and geophysical fluid dynamics phenomena such as tide-currents [23], pollutant dispersion [24], storm-surges or tsunami wave propagation [25]. Early work on numerical methods for solving the shallow water equations is described in Navon (1979) [26]. The test problem used in this paper is consisting of the nonlinear Shallow Water Equations (also called the Saint Venant equations [27]) in a channel on the rotating earth, associated with periodic boundary conditions in the x-direction and solid wall boundary condition in the y-direction:

$$u_t + uu_x + vu_y + \eta_x - fv = 0, \tag{24}$$

$$v_t + uv_x + vv_y + \eta_y + fu = 0, \tag{25}$$

$$\eta_t + (\eta u)_x + (\eta v)_y = 0, \tag{26}$$

$$u(0,y,t) = u(L_{\max},y,t),\ v(x,0,t) = v(x,D_{\max},t) = 0, \tag{27}$$

where $u(x,y,t)$ and $v(x,y,t)$ are the velocity components in the x and y axis respectively, $\eta(x,y,t)=gh(x,y,t)$ is the geopotential height, $h(x,y,t)$ represents the depth of the fluid, f is the Coriolis factor and g is the acceleration of gravity. Subscripts represent the derivatives with respect to time and the streamwise and spanwise coordinates.

We consider that the reference computational configuration is the rectangular 2D domain $\Omega=[0,L_{\max}]\times[0,D_{\max}]$. We consider the model (24-27) in a β-plane assumption [28,30], in which the effect of the Earth's sphericity is modeled by a linear variation in the Coriolis factor

$$f=\hat{f}+\frac{\beta}{2}(2y-D_{\max}), \tag{28}$$

where $\hat{f},\beta$ are constants, $L_{\max},D_{\max}$ are the dimensions of the rectangular domain of integration. The initial condition I1 introduced by Grammeltvedt [29] was adopted as the initial height field which propagates the energy in wave number one, in the streamwise direction:

$$h_0(x,y)=H_0+H_1\tanh\left(\frac{9(D_{\max}/2-y)}{2D_{\max}}\right)+H_2\sin\left(\frac{2\pi x}{L_{\max}}\right)\cosh^{-2}\left(\frac{9(D_{\max}/2-y)}{D_{\max}}\right). \tag{29}$$

Using the geostrophic relationship, $u=-h_y(g/f)$, $v=h_x(g/f)$, the initial velocity fields are derived as:

$$u_0(x,y)=-\frac{g}{f}\frac{9H_1}{2D_{\max}}\left(\tanh^2\left(\frac{9D_{\max}/2-9y}{2D_{\max}}\right)-1\right)-$$

$$\frac{18g}{f}H_2\sinh\left(\frac{9D_{\max}/2-9y}{D_{\max}}\right)\frac{\sin\left(\frac{2\pi x}{L_{\max}}\right)}{D_{\max}\cosh^3\left(\frac{9D_{\max}/2-9y}{D_{\max}}\right)}, \tag{30}$$

$$v_0(x,y)=2\pi H_2\frac{g}{fL_{\max}}\cos\left(\frac{2\pi x}{L_{\max}}\right)\cosh^{-2}\left(\frac{9(D_{\max}/2-y)}{D_{\max}}\right). \tag{31}$$

We have followed the approach used by Navon [28, 30], which implements a two-stage finite-element Numerov-Galerkin method for integrating the nonlinear shallow-water equations on a β-plane limited-area domain, for approximating the quadratic nonlinear terms that appear in the equations of hydrological dynamics. We have captured a number of 240 unsteady solutions of the two-dimensional shallow water equations model (24-27), with a time step of $\Delta t=600s$, while the dimensional constants used for the above model are

$$\hat{f}=10^{-4}s^{-1},\quad \beta=1.5\times10^{-11}s^{-1}m^{-1},\quad g=10ms^{-1}, \tag{32}$$

$$\mathrm{D}_{\max}=4400\mathrm{km},\quad \mathrm{L}_{\max}=6000\mathrm{km},\quad H_0=2000m,\quad H_1=220m,\quad H_2=133m. \tag{33}$$

In this section, the application of dynamic mode decomposition based on the reduced Schmid operator [1] is illustrated by comparing the evolution of the flow field along the integration time window in the cases of the full model and the reduced order model. The DMD spectra for the $(u,v,h)(x,y,t)$ fields are presented in Figure 15. The DMD technique presented herein is fully capable of determining the modal growth rates and the associated frequencies, which are illustrated in Figure 16, for geopotential height field h. Figure 17 presents the isolines of first right eigenvector and isolines of the first left eigenvector of the reduced Schmid operator, for the $(u,v,h)(x,y,t)$ fields. We perform the reconstruction of the $(u,v,h)(x,y,t)$ fields after 200 steps, corresponding to time $T=33.16h$, in Figure 18.

The DMD algorithm based on the reduced Schmid operator leads to a number of 173 modes retained for the reconstruction of geopotential height field, 42 modes retained for the reconstruction of the streamwise velocity field and 40 modes retained for the reconstruction of the spanwise

velocity field. In the case of DMD algorithm [2, 6], the number of stored modes is 192, 180, 151, respectively, thus a significant reduction in computational storage is achieved.

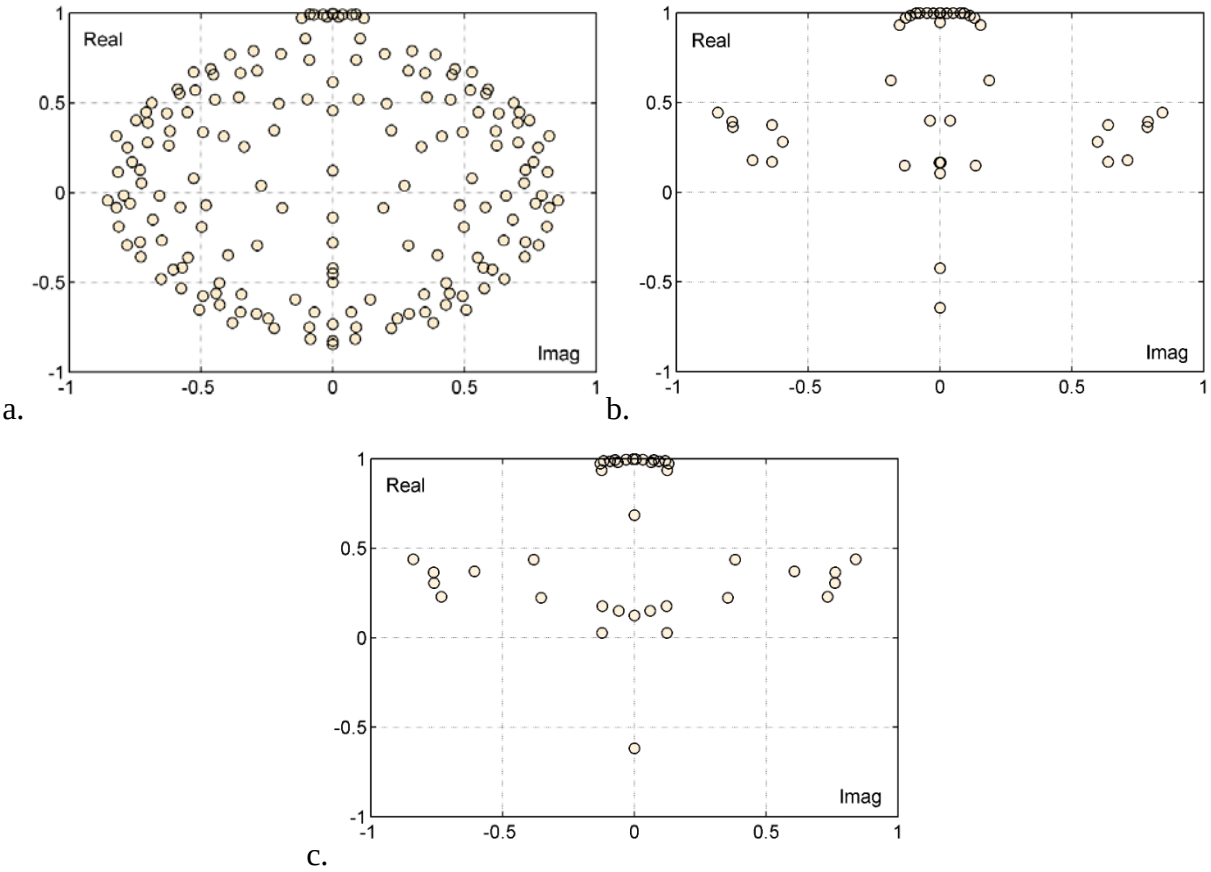

Figure 15. Spectrum of dynamic mode decomposition $\lambda_{\mathrm{Re}}(\lambda_{\mathrm{Im}})$ for (a) geopotential height field h, (b) streamwise velocity field u and (c) spanwise velocity field v, $\Delta t = 600s$.

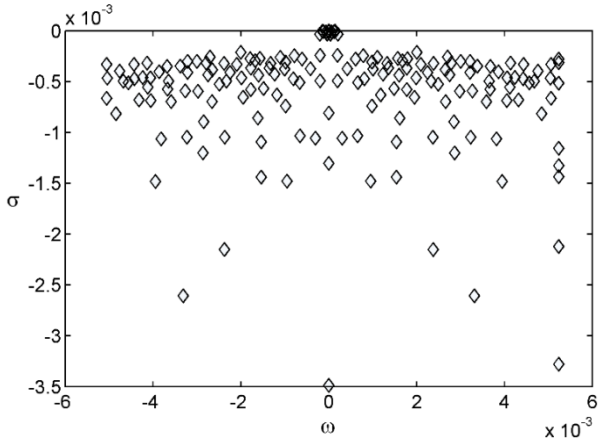

Figure 16. Growth rates and associated frequencies (σ, ω) obtained by dynamic mode decomposition of the geopotential height field h.

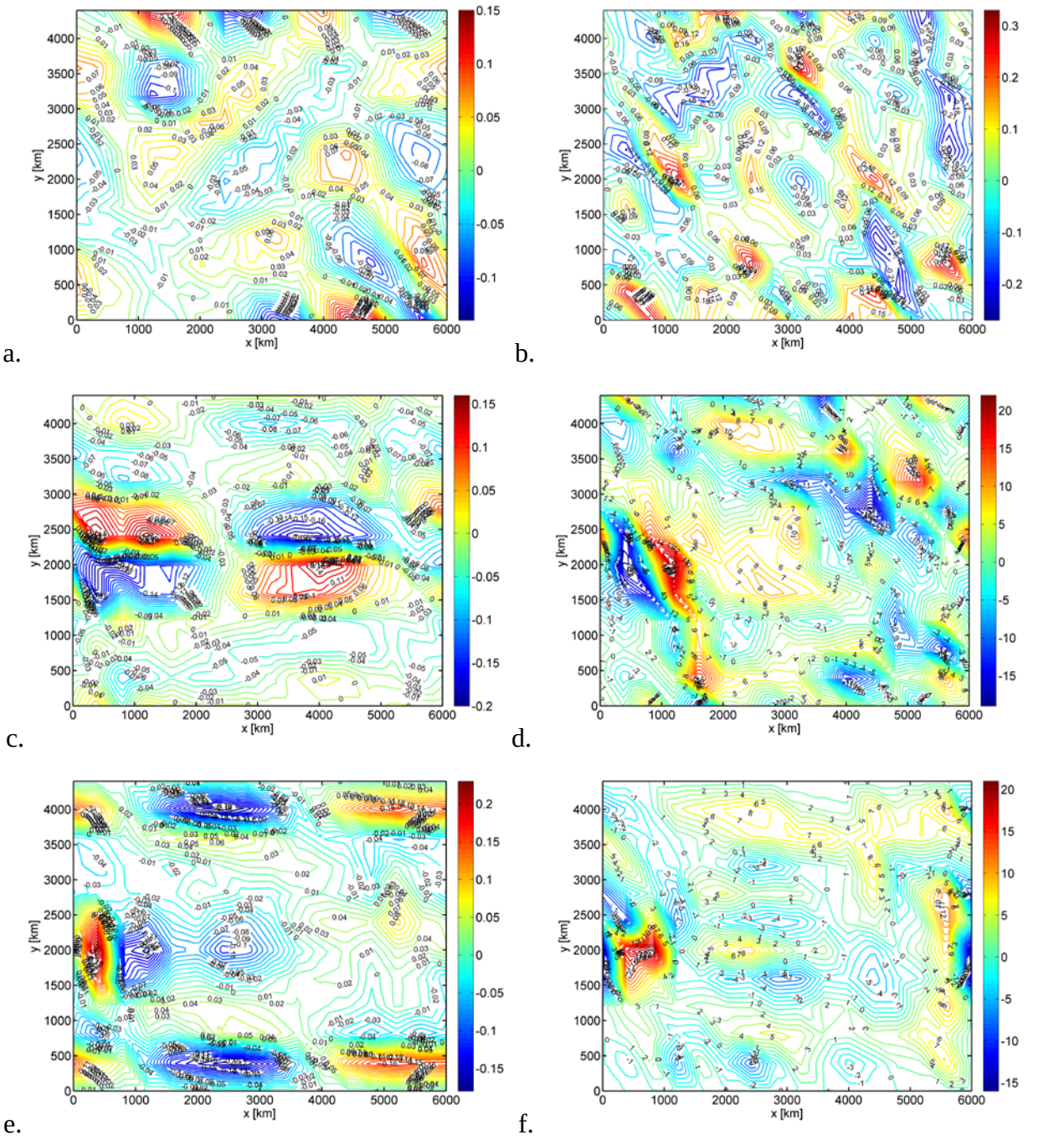

Figure 17. Isolines of the real right eigenvector (a, c, e) and isolines of the real left eigenvector (b, d, f) of the reduced Schmid operator, obtained by dynamic mode decomposition of the h,u,v fields, respectively.

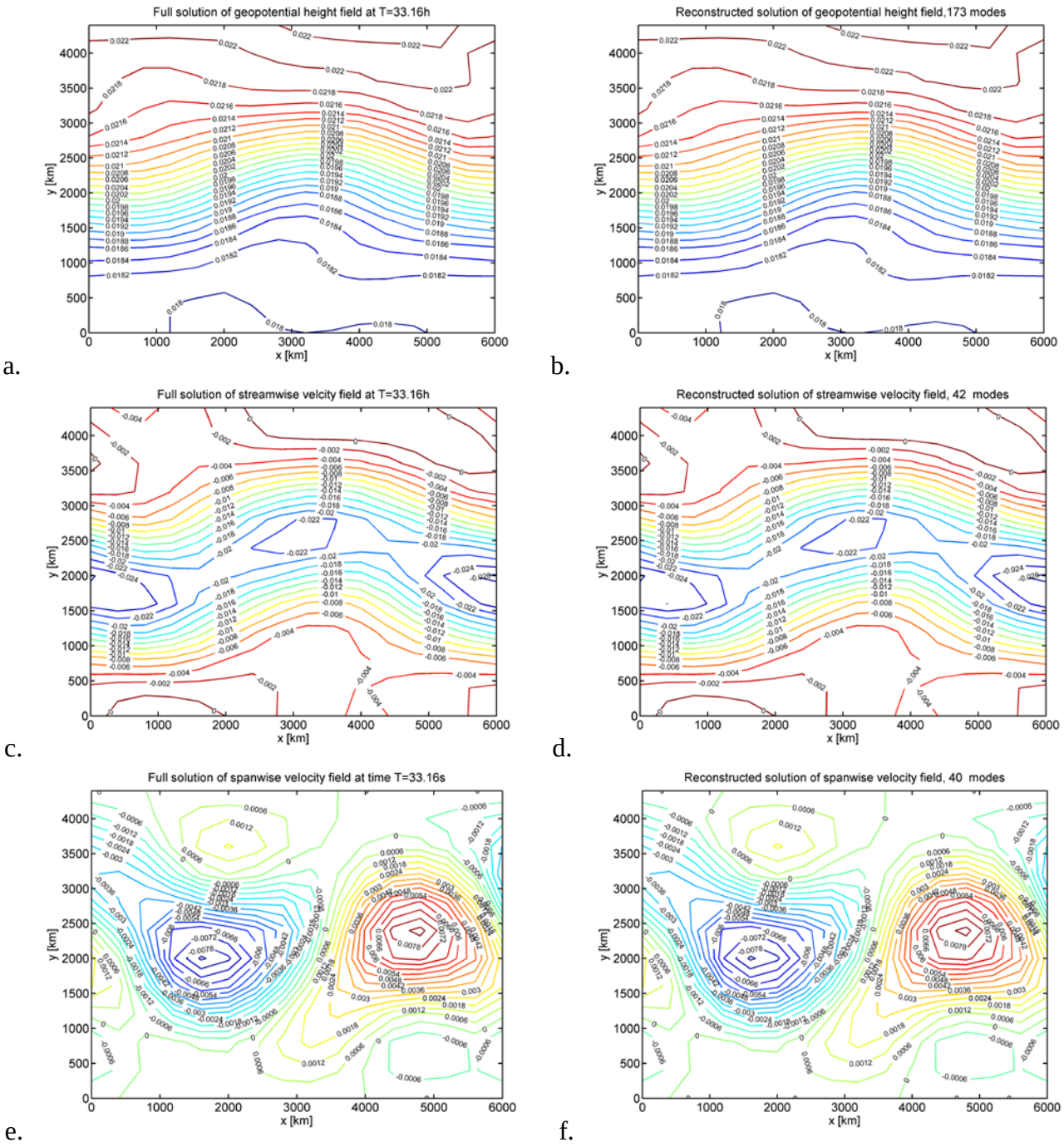

Figure 18. Reconstruction of h,u,v fields, respectively, employing the DMD based on reduced Schmid operator, at time $T = 33.16h$, $\Delta t = 600s$.

Selection of dynamic modes and amplitudes used for the flow reconstruction constitutes the source of many discussions among modal decomposition practitioners ([3, 6 and 31]). The superposition of all dynamic modes, weighted by their amplitudes and complex frequencies, approximates the entire data sequence, but there are also modes that have a weak contribution. On the other hand, the non-orthogonality of dynamic modes may raise the projection error while increasing the order of the DMD basis. To avoid these difficulties, we introduce in the following a numerical procedure to optimize the selection of dynamic modes involved in developing of a reduced order model of the flow. Assuming that, for the problem investigated here, there are no modes that are very rapidly damped having very high amplitudes, we explore the selection of the modes based on sorting them in decreasing order of their amplitudes. Based on the method of reduced Schmid operator presented herein, we retain dynamic modes and associated frequencies in descending order of their amplitudes until a minimum relative error of reconstruction is achieved.

We define the relative error as the L_2-norm of the difference between the variables of the full SWE model and approximate DMD solutions over the exact one, that is,

$$Er_{DMD} = \frac{\left\| w(x,y) - w_{DMD}(x,y) \right\|_2}{\left\| w(x,y) \right\|_2}, \tag{34}$$

where $w(x,y) \equiv (h,u,\mathrm{v})(x,y)$ represent the full solution of the SWE model and $w_{DMD}(x,y) \equiv (h_{DMD}, u_{DMD}, \mathrm{v}_{DMD})(x,y)$ represent the solution obtained by employing the optimized DMD based on the reduced Schmid operator.

We defer to a future study the investigation of other different techniques for identification of an optimal truncated representation of the flow field in order to capture the most important dynamic structures. The amplitudes of the optimized DMD modes function of the estimated frequencies, for h,u,v fields, respectively, are illustrated in Figure 19, where diamonds represent the retained modes after DMD optimization, circles represent discarded modes. After the optimized DMD is applied, the representation of the flow field is achieved retaining 19 modes for geopotential height field *h*, 28 modes for streamwise velocity field *u*, and 33 modes for spanwise velocity field *v*. The relative error computed as the retained number of dynamic modes is depicted in Figure 20. A comparison of the retained number of dynamic modes, in the case of classical DMD, DMD based on the reduced Schmid operator proposed in this paper and the optimized number of retained modes is presented in Table 2. A significant reduction of a factor of ten is achieved for the representation of geopotential height field, while the representation of the velocity field is improved by a factor of one and a half in computational resources.

The validity of the improved DMD approach introduced in this paper has been validated by comparing our results with those obtained by Stefanescu and Navon [32], when an alternating direction fully implicit (ADI) finite-difference scheme was used for discretization of 2-D shallow-water equations on a β-plane and the proper orthogonal decomposition (POD) coupled with discrete empirical interpolation (DEIM) was employed for the model reduction. In [32], the dimensions of POD bases for each variable was taken to be 35, while in the optimized DMD in the present approach we involve a smaller number of dynamic modes (see Table 2). The flow reconstructions presented in Figure 20 are very close to those computed in [32]. The similarity between these characteristics of the flow field and those obtained in the previous investigation validates the method presented here and certifies that the improved DMD method can be applied successfully to model reduction of 2-D flows. The relative error obtained by employing the optimized DMD based on the reduced Schmid operator in reconstruction of the flow fields is presented also in Table 2.

Table 2. The number of retained modes and relative error obtained by employing the optimized DMD based on the reduced Schmid operator.

Flow field	DMD method [2,6]	DMD based on reduced Schmid operator [1]	Optimized DMD based on reduced Schmid operator	Relative error Er_{DMD}
$h(x,y)$	192	173	19	0.0002683
$u(x,y)$	180	42	28	0.0016223
$v(x,y)$	151	40	33	0.0120628

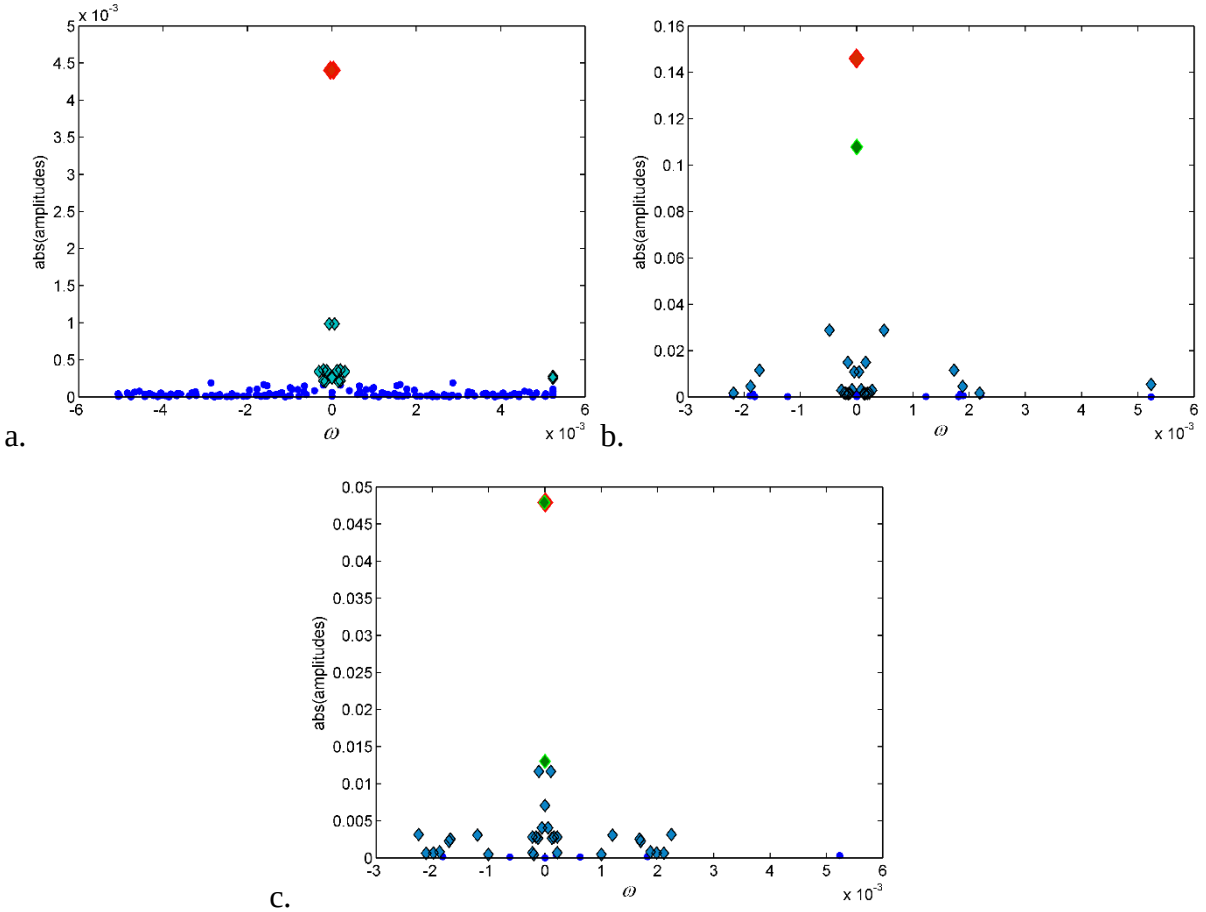

Figure 19. The amplitudes of the DMD modes as the estimated frequencies, for h,u,v fields, respectively, case of DMD based on the reduced Schmid operator. Diamonds represent the retained modes after DMD optimization, circles represent discarded modes.

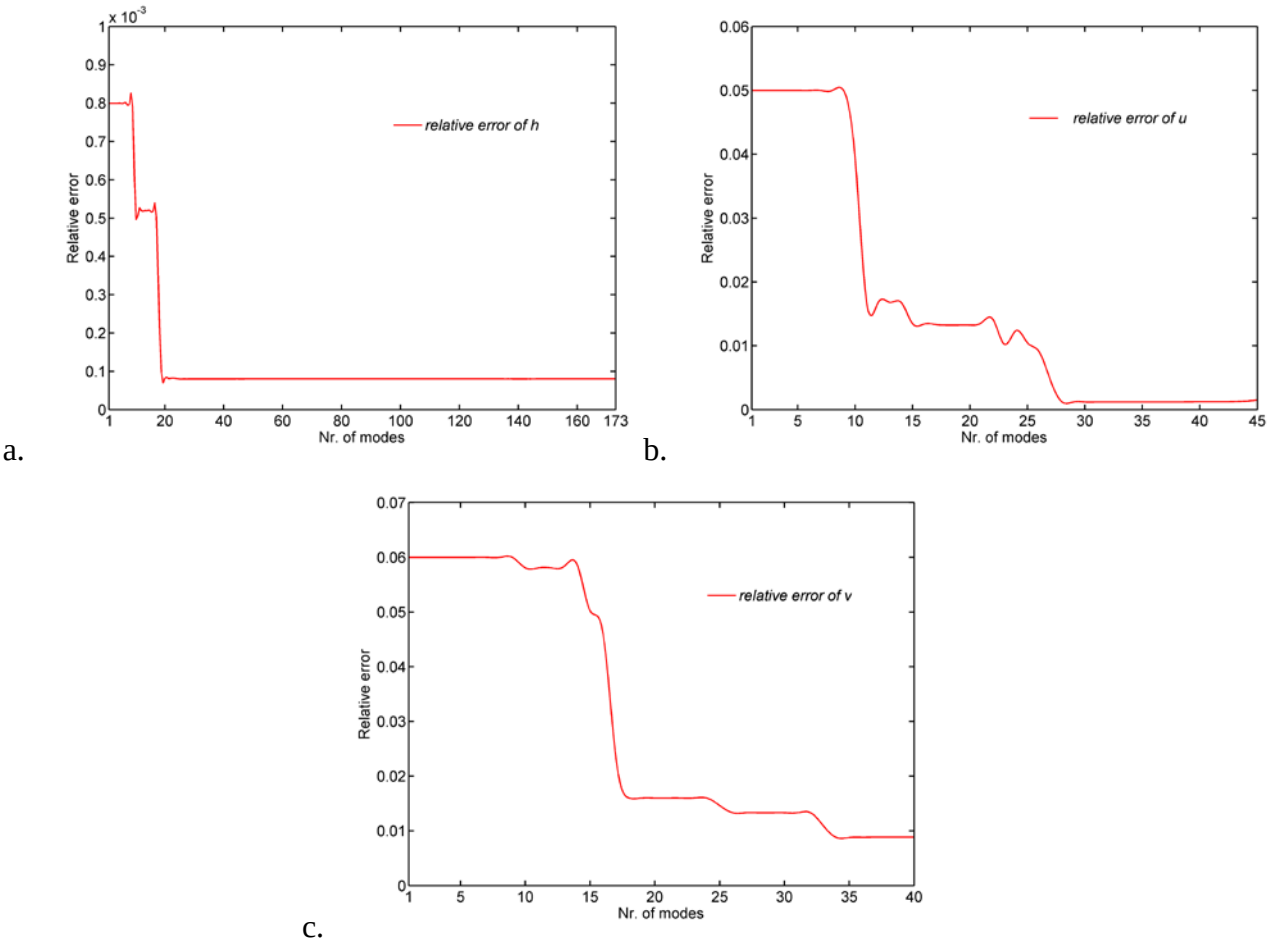

a. b. c.

Figure 20. The relative error computed as the retained number of dynamic modes, in case of optimized DMD based on the reduced Schmid operator, for h,u,v fields, respectively.

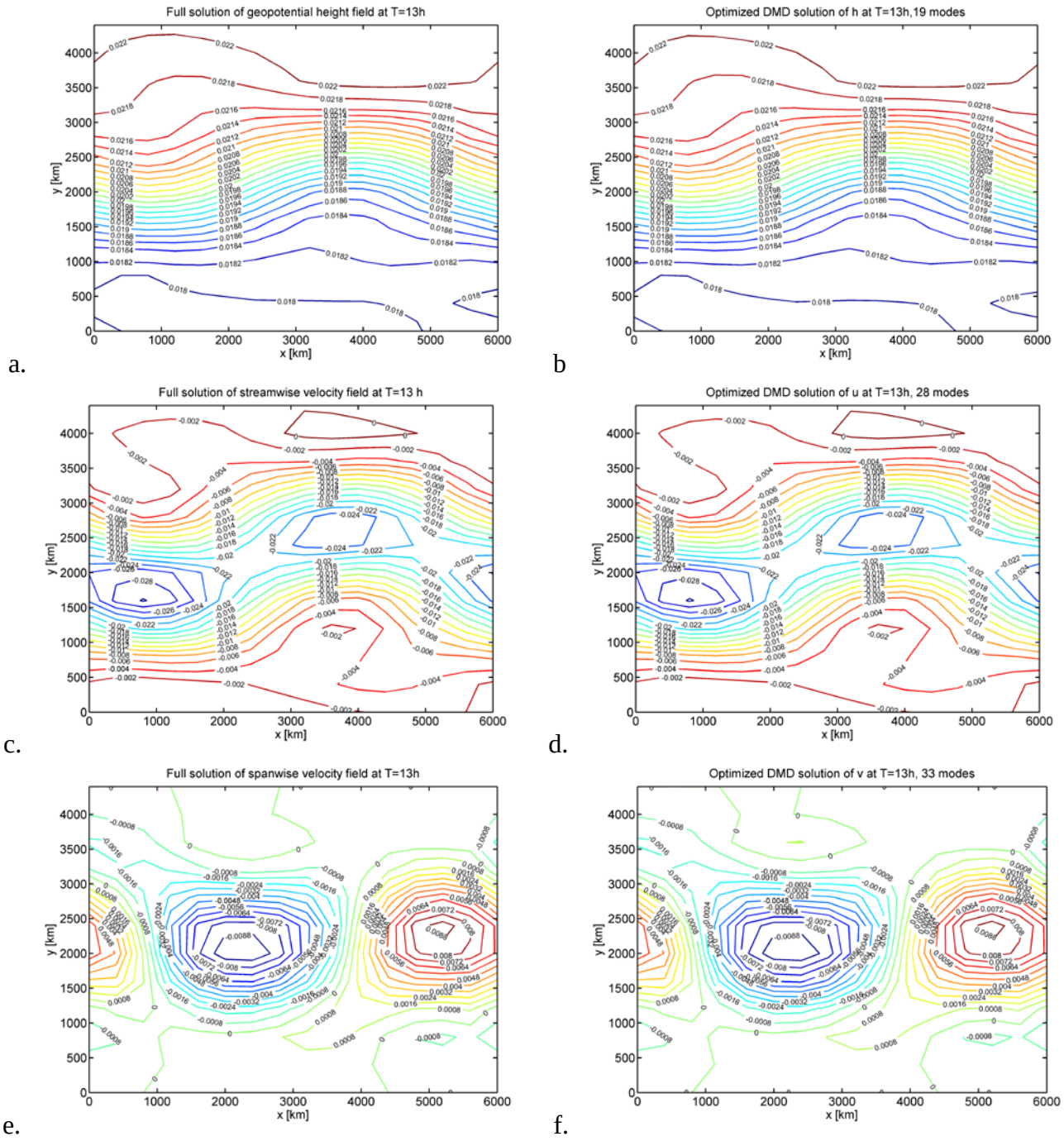

Figure 21. Reconstruction of h,u,v fields, respectively, employing the optimized DMD based on reduced Schmid operator, at time $T=13h$, $\Delta t=600s$. A significant reduction in retained number of dynamic modes is achieved.

6. SOME FEASIBLE APPLICATIONS OF THE SCHMID OPERATOR

The reduced form of the Schmid operator promises certain prospects in a set of additional applications.

6.1. Singular vectors

Disturbances, maximally growing for certain time interval, may be related to the eigenvectors of the operator composed of the product of forward and adjoint propagators [16].

The equation $du/dt = Bu$ in the linear approach may be resolved by the operator

$$u(\Delta t) = e^{B\Delta t}u_1 = Lu_1. \tag{35}$$

The norm of the solution assumes the form

$$\|u(\Delta t)\| = (Lu_1, Lu_1) = (u_1, L^* Lu_1)\,. \tag{36}$$

The search for maximally growing linear perturbations $\|u(\Delta t)\| / \|u_1\|$ at time interval Δt reduces to the search of eigenvectors $L^{*E} L\eta_{\max} = \sigma_{\max}^2 \eta_{\max}$ with the maximum eigenvalue $\sigma_{\max}^2$. The problem may be resolved iteratively using the action of the operator $A^* A$.

Under small enough time interval between snapshots, the Schmid operator is linear one that provides an opportunity for the calculation of singular vectors.

Figure 22 presents the singular vector for the impinging jet linear mode (the distance between snapshots (in steps) k=10, $\sigma_{\max}$=1.82), Figure 23 present the similar vector for the nonlinear mode (k=500, $\sigma_{\max}$=2.45).

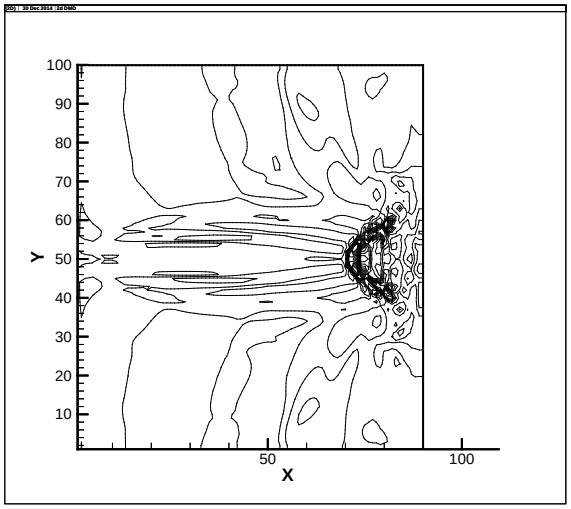

Figure 22. Isolines of singular vector (density component) in linear mode.

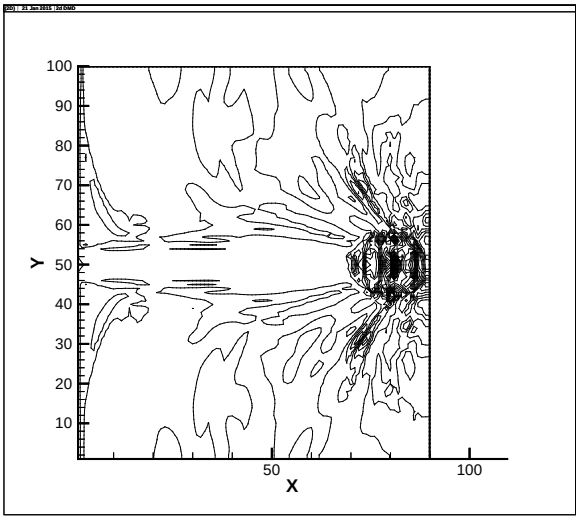

Figure 23. Isolines of singular vector (density component) in nonlinear mode.

Both the magnitude of eigenvalues and the shape of the eigenvectors (singular vectors) are quite different in linear and nonlinear events.

6.2 Receptivity

Eigenvectors of forward $A_{ji}(\Delta t)$ and adjoint propagators $A_{ij}^*(\Delta t)$ (Ω_R and Ω_L, correspondently) are biorthogonal that is important for the estimation of the flow receptivity to perturbations. It is known [15], that an initial disturbance should correspond to *k-th* mode of adjoint problem (Ω_L) in order to maximally excite the k-*th* mode of the forward problem. Thus, if right eigenvectors (dynamic modes) are useful at the search of main flow features, the left eigenvectors determine a receptivity of the flow to the external action.

The availability of left eigenvectors Ω_L enables estimation of the flow receptivity to initial field disturbances without applying an especial adjoint solver, such as used in Refs. [15, 16].

7. CONCLUSIONS

In this paper we have proposed a new framework for dynamic mode decomposition (DMD). The key innovation resides in application of the reduced Schmid operator instead of the classic DMD approach.

We proved that the Dynamic Mode Decomposition is equivalent to the Schmid operator approximation by a product of rectangular matrices of the right eigenvectors (dynamic modes), the left eigenvectors and the eigenvalue matrix. Instead of storing the total operator matrix, the proposed technique enables storing only two rectangular matrices and one diagonal matrix, that ensures computer memory and computing time (CPU) savings of about several orders of magnitude.

The main findings of our investigation are summarized in the following:

- the Schmid operator, on the same solution, may have either linear or nonlinear forms, in dependence on the time interval between snapshots;
- the Schmid operator in the linear limit may be of interest from the viewpoint of the estimation of receptivity and singular vectors.

In order to assess the performances of the proposed method, we have considered two numerical experiments: the case of a 2D supersonic underexpanded jet on a plate and the problem of the 2D shallow water equations. We applied the proposed DMD algorithm based on the reduced Schmid operator for different snapshots obtained by sampling down the original solutions of the full model with different time steps. We compared the novel DMD approach with the classic one in both cases.

Based on the DMD method introduced in [1], we proposed the optimization of DMD algorithm for reducing the number of dynamic modes retained for reconstructing the flow field. We arrange the modes in descending order of their amplitudes and we retain only the number of modes necessary for flow reconstruction with a minimum relative error. This procedure works well for models without modes that are very rapidly damped, having very high amplitudes. In these cases, different methods for retaining the modes shall be imposed and we defer this discussion to a future study.

We emphasized the excellent behaviour of the proposed optimized DMD method compared with the POD based model recent results existing in the literature [32]. Moreover, the model reduction technique proposed in this paper leads to a significant reduction in the number of retained modes, in comparison with the existing techniques. Additionally, we presented a rigorous error analysis for the reduced order models and we compared the relative computational efficiency of the aforementioned DMD technique.

ACKNOWLEDGEMENT

A.K. Alekseev and A.E. Bondarev acknowledge the partial support by grants of RFBR № 13-01-00367A and № 14-01-00769A. D.A. Bistrian acknowledges the partially support of strategic grant POSDRU/159/1.5/S/137070 (2014) of the Ministry of National Education, Romania, co-financed by the European Social Fund-Investing in People, within the Sectorial Operational Program Human Resources Development 2007-2013. Prof. I.M. Navon acknowledges the support of NSF grant ATM-0931198.

REFERENCES

1. Schmid PJ. Dynamic mode decomposition of numerical and experimental data. *Journal of Fluid Mechanics* 2010; **656.1**: 5-28.
2. Rowley CW, Mezic I, Bagheri S, Schlatter P, and Henningson DS. Spectral analysis of nonlinear flows. *Journal of Fluid Mechanics* 2009; **641**:115-127.

3. Chen KK, Tu JH, and Rowley CW. Variants of dynamic mode decomposition: boundary condition, Koopman, and Fourier analyses. *J. Nonlinear Sci*. 2012; **22**: 887–915.
4. Guéniat F, Mathelin L, and Pastur LR. A dynamic mode decomposition approach for large and arbitrarily sampled systems. *Phys. of Fluids* 2015; **27:** 025113.
5. Jovanovic MR, Schmid PJ, and Nichols JW. Sparsity-promoting dynamic mode decomposition. *Phys. of Fluids* 2014; **26:** 024103.
6. Bistrian DA and Navon IM, An improved algorithm for the shallow water equations model reduction: Dynamic Mode Decomposition vs POD. *International Journal for Numerical Methods in Fluids* 2015; **79**(9): 552--580.
7. Holmes P, Lumley JL, Berkooz G. *Turbulence, Coherent Structures, Dynamical Systems and Symmetry*. Cambridge Univ. Press.: New York, 1996.
8. Bagheri S. Koopman-mode decomposition of the cylinder wake. *Journal of Fluid Mechanics* 2013; **726**:596–623.
9. Mezic I. Analysis of fluid flows via spectral properties of the Koopman operator. *Annual Review of Fluid Mechanics*2013; **45**(1):357–378.
10. Tu JH, Rowley CW, Luchtenburg DM, Brunton SL, Kutz JN. On dynamic mode decomposition: theory and applications.*Journal of Computational Dynamics* 2014; **1**(2):391-421.
11. Hemati MS, Williams MO, Rowley CW. Dynamic mode decomposition for large and streaming datasets. *Physics of Fluids* 2014; **26**:111701; doi: 10.1063/1.4901016
12. Williams MO, Rowley CW, Mezic I, Kevrekidis IG. Data fusion via intrinsic dynamic variables: An applicationof data-driven Koopman spectral analysis. *EPL* (*Europhysics Letters)* 2015; **109**(4): 40007; doi:10.1209/0295-5075/109/40007
13. Koopman B, Hamiltonian systems and transformations in Hilbert space. *Proc. Nat. Academy of Sciences of the USA* 1931; **17**: 315-318.
14. Lan YH, Mezic I. Linearization In the Large of Nonlinear Systems and Koopman Operator Spectrum. *Physica D-nonlinear Phenomena* 2013; **242:** 42–53.
15. Hill DC. Adjoint systems and role in the receptivity problem for boundary layers. *J. Fluid Mech*. 1995; **292**: 183-204.
16. Farrell BF and Moore AM. An adjoint method for obtaining the most rapidly growing perturbation to oceanic flows. *J. Phys. Oceanogr*. 1992; **22:** 338-349.
17. Golub GH, Van Loan Ch. *Matrix computations*. JHU Press, 1996.
18. Pundir B and Dhanak M. Surface Pressure Fluctuations Due to an Impinging Supersonic Underexpanded Jet. AIAA 2010-107, p 1-13.
19. van Leer B. Towards the ultimate conservative difference scheme. V. A second-order sequel to Godunov's method. *J. Comput. Phys*. 1979; **32**: 101–136.
20. Sun M, Katayama K. An artificially upstream flux vector splitting for the Euler equations. *J. Comput. Phys*. 2003; **189:** 305-329.
21. Anderson E, Bai Z, Bischof C, Blackford S, Demmel J, Dongarra J, Du Croz J, Greenbaum A, Hammarling S, McKenney A, and Sorensen D. *LAPACK Users' Guide, Third Edition.* SIAM, 1999.
22. Lehoucq RB, Sorensen DC, Yang C. *ARPACK Users Guide: Solution of Large-Scale Eigenvalue Problems with Implicitly Restarted Arnoldi Methods*. SIAM, 1998.
23. Bryden IG, Couch SJ, Owen A, Melville G. Tidal current resource assessment. *Proc. IMechE Part A: J. Power and Energy*2007; **221**:125--135.
24. Sportisse B, Djouad R. Reduction of chemical kinetics in air pollution modeling. *Journal of Computational Physics* 2000; **164**:354--376.
25. Koutitus C. *Mathematics models in coastal engineering*. Pentech Press, London, 1988.
26. Navon IM. *Numerical methods for the solution of the shallow-water equations in Meteorology*. University of the Witwatersrand, Johannesburg (South Africa), PhD Thesis, available from ProQuest, UMI Dissertations Publishing, 1979. 0533651.

27. Vreugdenhil CB. *Numerical Methods for Shallow Water Flow*. Kluwer Academic Publishers, 1994.
28. Navon IM. *A* Numerov-Galerkin Technique Applied to a Finite-Element Shallow Water Equations Model with Enforced Conservation of Integral Invariants and Selective Lumping. *Journal of Computational Physics*1983; **52**, 313--339 .
29. Grammeltvedt A. A survey of finite-difference schemes for the primitive equations for a barotropic fluid. *Monthly Weather Review*1969; **97**(5):384--404.
30. Navon IM. FEUDX: A two-stage, high accuracy, finite-element FORTRAN program for solving shallow-water equations. *Computers and Geosciences*1987; **13**(3):255--285.
31. Jovanovic MR, Schmid PJ, Nichols JW. Low-rank and sparse dynamic mode decomposition. *Center for Turbulence Research Annual Research Briefs* 2012; 139--152.
32. Stefanescu R, Navon IM. POD/DEIM nonlinear model order reduction of an ADI implicit shallow water equations model. *Journal of Computational Physics* 2013; **237**:95-114.